Multisource inverse-geometry CT. Part I. System concept and development

Bruno De Man[a)]
CT Systems and Applications Laboratory, GE Global Research, Niskayuna, New York 12309

Jorge Uribe
Functional Imaging Laboratory, GE Global Research, Niskayuna, New York 12309

Jongduk Baek
School of Integrated Technology, Yonsei University, Incheon 406-840, South Korea

Dan Harrison and Zhye Yin
CT Systems and Applications Laboratory, GE Global Research, Niskayuna, New York 12309

Randy Longtin and Jaydeep Roy
Mechanical Systems Technologies, GE Global Research, Niskayuna, New York 12309

Bill Waters
Design and Development Shops, GE Global Research, Niskayuna, New York 12309

Colin Wilson
High Energy Physics Laboratory, GE Global Research, Niskayuna, New York 12309

Jonathan Short
Detector Laboratory, GE Global Research, Niskayuna, New York 12309

Lou Inzinna
High Energy Physics Laboratory, GE Global Research, Niskayuna, New York 12309

Joseph Reynolds
High Frequency Power Electronics Laboratory, GE Global Research, Niskayuna, New York 12309

V. Bogdan Neculaes
High Energy Physics Laboratory, GE Global Research, Niskayuna, New York 12309

Kristopher Frutschy
Mechanical Systems Technologies, GE Global Research, Niskayuna, New York 12309

Bob Senzig
Molecular Imaging and Computed Tomography, GE Healthcare, Waukesha, Wisconsin 53188

Norbert Pelc
Department of Radiology, Stanford University, Stanford, California 94305

(Received 20 November 2015; revised 16 May 2016; accepted for publication 15 June 2016; published 18 July 2016)

Purpose: This paper presents an overview of multisource inverse-geometry computed tomography (IGCT) as well as the development of a gantry-based research prototype system. The development of the distributed x-ray source is covered in a companion paper [V. B. Neculaes *et al.*, "Multisource inverse-geometry CT. Part II. X-ray source design and prototype," Med. Phys. **43**, 4617–4627 (2016)]. While progress updates of this development have been presented at conferences and in journal papers, this paper is the first comprehensive overview of the multisource inverse-geometry CT concept and prototype. The authors also provide a review of all previous IGCT related publications.
Methods: The authors designed and implemented a gantry-based 32-source IGCT scanner with 22 cm field-of-view, 16 cm z-coverage, 1 s rotation time, 1.09×1.024 mm detector cell size, as low as 0.4×0.8 mm focal spot size and 80–140 kVp x-ray source voltage. The system is built using commercially available CT components and a custom made distributed x-ray source. The authors developed dedicated controls, calibrations, and reconstruction algorithms and evaluated the system performance using phantoms and small animals.
Results: The authors performed IGCT system experiments and demonstrated tube current up to 125 mA with up to 32 focal spots. The authors measured a spatial resolution of 13 lp/cm at 5% cutoff. The scatter-to-primary ratio is estimated 62% for a 32 cm water phantom at 140 kVp. The authors scanned several phantoms and small animals. The initial images have relatively high noise due to the low x-ray flux levels but minimal artifacts.

Conclusions: IGCT has unique benefits in terms of dose-efficiency and cone-beam artifacts, but comes with challenges in terms of scattered radiation and x-ray flux limits. To the authors' knowledge, their prototype is the first gantry-based IGCT scanner. The authors summarized the design and implementation of the scanner and the authors presented results with phantoms and small animals.
[http://dx.doi.org/10.1118/1.4954846]

Key words: computed tomography, inverse-geometry CT, multisource CT

1. INTRODUCTION

Soon after the conception of computed tomography (CT) in the late 1960s and early 1970s, the third-generation CT architecture was introduced. Even today, it forms the basis for almost all CT scanners, including systems with multiple beam lines.[1–4]

The earliest inverse-geometry CT (IGCT) reference dates back to 2002 by Xu.[5] In 2004, Schmidt *et al.* reported an IGCT architecture based on a scanned area x-ray source and a small photon-counting detector.[6] One of the motivations of this system was to provide artifact-free large volumetric coverage, by distributing the x-ray generation not only laterally but also longitudinally.[7] Moreover, the high-efficiency photon-counting detector and the relatively scatter-free geometry would also make a very dose-efficient concept. Experimental demonstration was reported in Ref. 8, combining an existing inverse-geometry *x-ray* system[9,10] with a rotating stage to obtain an IGCT table-top system.

A related approach (multisource CT) combines two or more laterally offset x-ray sources with a small detector. The discrete x-ray sources can be operated in a *virtual bowtie* mode, which consists of differentially controlling the flux from each source, as explained in detail in Sec. 2.C.[11]

The above concepts are specific cases of a larger class of CT architectures: a traditional third-generation CT system can morph into a fully inverted CT system by increasing the number of discrete x-ray sources and decreasing the detector size. Vice versa, a fully inverted CT system can morph into a third-generation CT system by increasing the number of discrete detector eyes and reducing the x-ray panel source size.

This realization led to the collaborative development of a gantry-based IGCT prototype, funded in part by the NIH NIBIB (acknowledged below) and in part by General Electric. We previously presented the development of multisource reconstruction methods[12–20] and calibration methods.[21–24] Several progress updates on the system development and initial results were published in Refs. 25–32. This paper summarizes the concept of IGCT and gives a comprehensive overview of the completed gantry-based IGCT prototype and experimental results. The distributed x-ray source developments are referred to in the companion paper.[44]

2. METHODS

2.A. Basic concept

The basic concept of inverse geometry CT is best explained in 2D. CT projection line measurements can be represented in polar coordinates: θ is the angle the projection ray makes with the vertical (y-) axis and r is the radial coordinate or the *signed* orthogonal distance between the ray and the origin (we add a minus sign if the origin is to the left of the ray as seen by the x-ray source). In Fig. 1, we show the image space sampling on the left and the Radon space sampling on the right. Each projection line in image space corresponds to a single point in Radon space. Each collection of projection lines in image space corresponds to a line segment in Radon space. The bold lines in image space correspond to the dots in Radon space.

Figure 1(a) shows the first-generation CT acquisition scheme, based on the translate-rotate principle: source and detector are translated across the field-of-view (FOV) repeatedly for all projection angles, so r ranges from $-$ FOV/2 to FOV/2 and θ ranges from 0° to 360°. Figure 1(b) shows the second-generation CT acquisition scheme, with multiple detector channels. It still requires translation across the FOV, but fewer rotation steps are needed. Figure 1(c) shows a third-generation CT acquisition scheme, in which all projection lines converge at the x-ray source and cover the entire FOV, to eliminate the need for translation. This scheme is the basis for essentially all existing commercial CT scanners. Figure 1(d) shows a typical inverse-geometry CT acquisition scheme with a finite detector size. This is the topology used in the experimental prototype described in this paper.

All above acquisition schemes measure the same complete set of projection lines, but in a different order. If multiple x-ray sources are activated simultaneously and irradiate the same detector channel(s), reconstruction becomes highly ill-posed, leading to increased noise and image artifacts.[27] By design, we only activate one x-ray source at a time, although it is conceivable that multiple x-ray sources could be activated simultaneously, sending x-rays to nonoverlapping detector sections.

The x-ray source and detector also have a z-dimension: in the experimental IGCT scanner described in this paper, the x-ray source consists of two rows of focal spots that are offset longitudinally and the detector is a multirow detector.

2.B. System development

The major parameters of the multisource IGCT scanner are summarized in Table I. The scanner includes an x-ray source array within a single vacuum chamber holding all x-ray sources arranged in two rows separated 100 mm longitudinally with 16 focal spots per row.

The x-ray chamber (including cooling system, high voltage generator, and vacuum pumps), the detector, and their

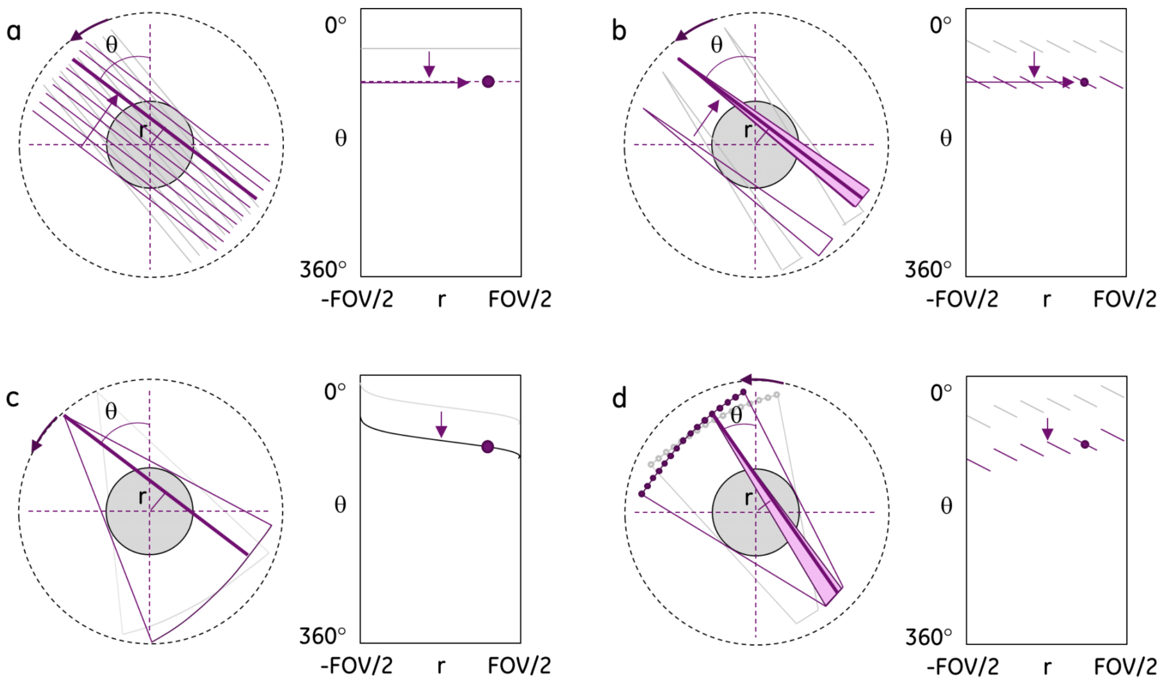

FIG. 1. Comparison of various CT acquisition schemes, from top to bottom: first-generation CT, second-generation CT, third-generation CT, and IGCT.

supporting electronics and controls are mounted on a rotating gantry. Figure 2 shows the mechanical design drawings of the IGCT scanner and Fig. 3 shows a picture of the IGCT scanner.

The majority of the supporting components are parts from standard clinical CT systems (Lightspeed VCT and Discovery CT 750HD, GE Healthcare, Waukesha, WI) and modifications of such components. Specifically, the detector array and front-end electronics are based on Discovery CT 750HD detector modules.

Twelve detector modules were stacked longitudinally, each with 64×16 detector cells with cell size 1.09×1.024 mm for a total detector size of 7×19.7 cm (with the in-plane dimensions shown first).

A number of mechanical fixtures and supporting brackets were designed specifically for this IGCT scanner. The mechanical solid model of the system (Fig. 2) is the result of several iterations of arranging the new components around existing hardware in order to minimize re-engineering of the rotating base supporting all rotating components. Even though the imaging field-of-view is only 22 cm, the source vessel is rather bulky ($55\times53\times29$ cm). We estimate that a next-generation distributed x-ray source could be designed as a more compact cylindrical vacuum vessel on the order of 30 cm in diameter and 70 cm in length while covering a full 50 cm FOV in combination with a 50×20 cm active detector area. Hence, the gantry size for an MS-IGCT system would be roughly comparable to today's commercial scanners.

TABLE I. Summary of major system and acquisition parameters of the gantry-based IGCT scanner.

Tube voltage	80, 100, 120, 140 kVp
Tube current	Tested up to 125 mA
Dwell time	10–100 μs
Focal spot x and z size	As low as 0.4×0.8 mm
Source columns and rows	16×2 (4×2 in phase 1)
Source physical size	375×100 mm
Detector cell x and z size	1.09×1.024 mm
Detector columns and rows	64×192
Detector physical size	70×197 mm
Source-to-isodistance	450 mm
Detector-to-isodistance	385 mm
Z-coverage	160 mm
FOV	220 mm (75 mm in phase 1)

The system was designed to rotate as fast as 1 s per rotation. Five weight stacks distributed around the rotating base were designed to provide precise balancing of the gantry. Their locations and nominal values were determined analytically based on detailed knowledge of all mechanical components (weights and centers of mass) and their location on the gantry. Fine-tuning of the weight stacks was achieved using piezoelectric strain gauges attached to the gantry's legs and calculating residual dynamic imbalance during gantry rotation.

High voltage for the x-ray sources was generated with a positive polarity high voltage generator (140 kVp max). The high-voltage cable connecting the generator to the vacuum chamber is significantly longer than the cable in a conventional system in order to maximize internal capacitance. This large capacitance in the cable helps to reduce voltage droop caused by the on-switching of the x-ray sources. Typical source operating parameters were 80 kV and 125 mA, with each source pulsed individually for 10–100 μs. High-voltage electrical discharges in the vacuum enclosure occurred initially due to outgassing of components, but their frequency decreased with continued use of the sources. High vacuum ($\sim10^{-7}$ Torr or better) was required to avoid these discharges during normal operation. In order to maintain the appropriate

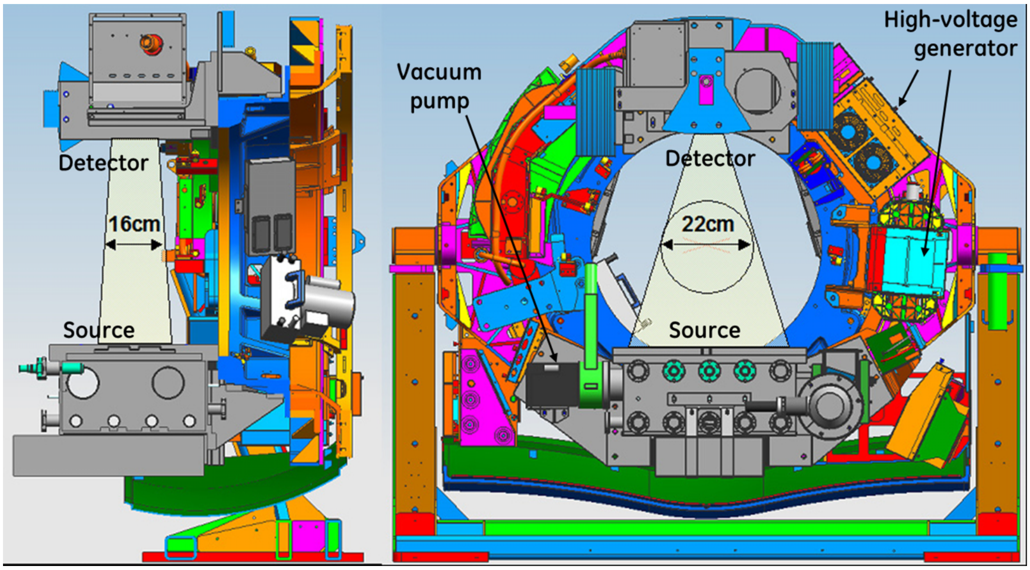

FIG. 2. Mechanical design drawings for the IGCT scanner, illustrating 22 cm FOV, 16 cm z-coverage, and the location of major hardware components (Reprinted with permission from De Man *et al.*, "Multi-source inverse-geometry CT: From system concept to research prototype," in IEEE Nuclear Science Symposium and Medical Imaging Conference, Orlando, Florida, 2009. Copyright 2009 IEEE).

vacuum level, active pumping of the chamber was provided during rotation of the gantry. An ion pump (75 l/s) provided suitable vacuum during rotation. Initial creation of the vacuum in the chamber was assisted with a turbo pump (250 l/s) connected to a valve-controlled second port on the chamber; this component was mechanically disconnected during gantry rotation.

The system utilizes a stationary-anode design—each electron beam impinges upon the same location of the anode during x-ray exposure. Due to the risk of melting the tungsten anode surface, x-ray flux is limited in a stationary-anode x-ray tube design. To allow higher beam currents and higher duty cycle, we designed active cooling to the anode from a heat exchanger mounted on the rotating gantry. However, active cooling was not used for the experiments presented in this paper, because the scan times were relatively short and the number of scans per day was limited. Each focal spot in a distributed x-ray source needs its own x-ray beam collimation. Our source is self-collimated by the shroud surrounding the x-ray target. In addition, we designed a relatively simple two-layer collimation scheme (2 mm *W* at the shroud and 2 mm *W* outside the chamber) that could be implemented for improved beam collimation, but has not been implemented at this stage. High-frequency, high-voltage switching electronics were developed in-house for this IGCT system. The electronics board (in its casing) is attached to the vacuum chamber. Special care was taken to design internal protections to quench high-voltage electrical discharges while maintaining fast transitions at high switching speeds. The details of the x-ray generation are described in detail in the companion paper.[44]

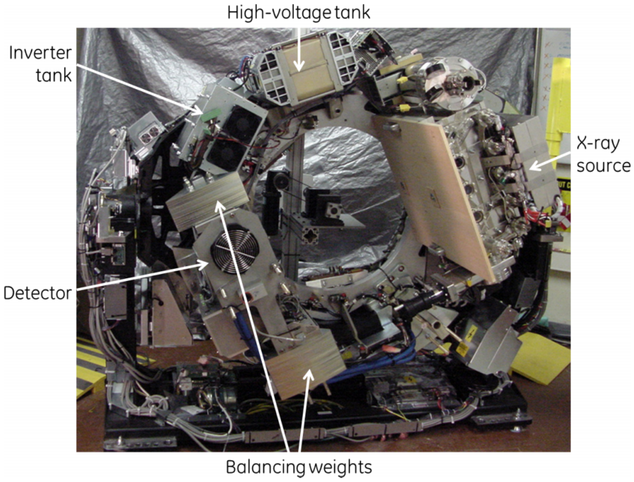

FIG. 3. Picture of the IGCT scanner with the gantry parked, showing some of the major components.

2.C. Virtual bowtie

One of the main motivations for this work is to minimize patient radiation dose through the use of an *electronic* or *virtual bowtie*. Since each x-ray beam is relatively narrow, we have finer control of the number of x-rays sent through different regions of the patient than with the traditional third-generation geometry. Each x-ray beam contributes to important imaging information: the contrast-to-noise ratio will improve in regions that are *interrogated* with more x-rays. At the same time, each x-ray beam also deposits radiation dose to the patient, so we want to tailor the x-ray distribution based on the local anatomical context. It is desired to send more x-rays along path lengths with higher accumulated attenuation and in regions of great diagnostic interest and to avoid sending x-rays directly to sensitive organs. Eventually we would like to define a complete x-ray pulse sequence, including source index, pulse start time, pulse duration, x-ray source voltage, and x-ray source beam current. An initial mathematical framework called computer assisted scan protocol and reconstruction (CASPAR) has been developed.[33,34]

Quantitative estimates of the dose reduction potential of the virtual bowtie strongly depend on the anatomy. Bartolac *et al.*[35] showed examples where, compared to using a fixed bowtie, fluence field optimization achieved superior agreement with the target image quality objectives and resulted in integral dose reductions ranging from 39% to 52%. Experiments by Szczykutowicz and Mistretta[36] suggest up to 3.6 times dose reduction relative to "flat field" CT. We have recently performed an experiment with a dynamic, aggressive bowtie[37] focusing on a cardiac ROI and avoiding a spine ROI, resulting in an estimated spine dose reduction of up to 6×. The results in Ref. 34 are most directly applicable to the virtual bowtie. We conclude that protocol optimization for third-generation CT yields an improvement of more than 50%. For a virtual bowtie with five subfans, the dose/variance is reduced by 83%. By increasing the number of subfans, 86% is achieved. Based on all the above, we estimate that the virtual bowtie would result in tens of % dose reduction in most clinical applications, but 6–8× organ dose reduction is possible in highly targeted region-of-interest imaging. While we have not performed an extensive virtual bowtie system-level study on the IGCT prototype scanner, one virtual bowtie experiment is described in the companion paper.[44]

2.D. System calibration

Geometric calibration for every CT system design is an important step to produce high-quality CT images. In IGCT, geometric calibration has additional challenges since the coordinates of all x-ray sources need to be estimated, and any inaccuracies in their estimation will result in perceived inconsistencies in the data, which are then amplified by the reconstruction filter and may cause severe image artifacts. The relative position of the detector, rotation axis, and the 32 focal spots was determined using a 4 cm diameter PMMA cylinder, with five beads placed on the surface, separated by 2 cm along the axis of the cylinder. To further reduce the estimation error, a 200 μm diameter tungsten wire phantom was scanned and the estimated parameters were readjusted to maximize the reconstructed value of the wire. More details on the geometric calibration are given in Refs. 22 and 23.

A second type of calibration that is particularly important for IGCT is the flux calibration. Even though we control the voltage, dwell time, and current of each x-ray pulse, the actual intensity will always have some deviation from its nominal value, again leading to possible inconsistencies in the projection data. Conventional CT scanners monitor intensity fluctuations using reference channels at the edges of the detector (outside the projection of the FOV), but in an IGCT geometry, most sources do not irradiate the reference detectors without going through the scanned object. We developed a data normalization technique to correct for the IGCT intensity fluctuations,[24] essentially making sure that adjacent patches of projection data are consistent by slightly rescaling their intensities. The projection data of adjacent focal spots in the IGCT system share an overlap region in Radon space. That overlap corresponds to a 3-fold redundancy of the measurements. We defined a set of unknown gain factors for all views to compensate for the intensity fluctuations and compute these from the redundant measurements. We used the projection data of the source irradiating the outermost FOV as a reference for data normalization.[24]

Other types of calibration and correction are similar to conventional CT systems. Beam hardening and spectral nonlinearity of the detector were corrected based on uniform cylindrical phantoms, using a second order polynomial fit between the analytic projection data and the real scan data.[38]

2.E. Multisource reconstruction

In 2D, multisource inverse-geometry CT acquires exactly the same projection lines as third-generation CT (after rotation over 360°), so we can use rebinning to transform the multisource dataset to a third-generation dataset or to a parallel-beam dataset. In 3D, the situation is more complex: if the x-ray sources are distributed in-plane (transaxially) along an isocenter-focused arc, all partial cone-beams can be virtually rotated such that they jointly form a third-generation CT dataset. Since the sources in the IGCT system are distributed along two straight lines rather than on two isocentered arcs, the above condition does not hold, and the rebinning process will introduce some errors. Since two rows of x-ray focal spots are used, two longitudinally offset third-generation CT acquisitions are obtained after rebinning. Each axial acquisition is reconstructed using the FDK (Feldkamp, Davis and Kress) algorithm.[39] The contributions from both source rows are merged in the image domain using a gradual weighting scheme to achieve the final reconstructed volume: a tapered weighting scheme is used with three plateaus at 0, 0.5, and 1.0 and a linear transition region between the plateaus.[22] The system geometry is such that the contributions from both source rows share a substantial overlap volume, which corresponds to the plateau at 0.5 in the weighting scheme. More advanced cone-beam reconstruction schemes such as used in industry[40] could be used to further refine the tradeoff between cone-beam artifacts and image noise.

We have developed several alternate *multiaxial* reconstruction algorithms that could be applied to further reduce cone-beam artifacts. Since they were not used in the experiments described in this paper, we are not including a description but refer to the respective publications.[12,13,15,18,20]

3. RESULTS AND DISCUSSION

3.A. Detector efficiency

By the nature of an inverse-geometry CT architecture, its detector has significantly smaller overall dimensions than a detector used in third-generation CT. Transaxially, the IGCT detector is typically selected to be about 10–20 cm or up to 50 cm for the balanced design. Longitudinally, an IGCT system with two source rows can achieve a given coverage with a smaller detector dimension than a third-generation CT system, since the magnification effect is eliminated. The reduced detector size is an obvious system cost benefit, but the increased x-ray source complexity makes the overall system cost comparable to a third-generation CT architecture. Since x-rays reaching the detector originate from different *trans*axial positions, an in-plane antiscatter grid (postpatient collimator) is not recommended. Similarly, in the case of multiple rows of x-ray focal spot, an antiscatter grid in z is not desired either. Fortunately, the much smaller solid angle subtended by x-ray beam will naturally result in lower scattered radiation—to first-order approximation, the scatter-to-primary ratio (SPR) is proportional to the solid angle. Ideally, an IGCT system should maintain acceptable SPR levels, despite the absence of an antiscatter grid. In practice, the detector size and the corresponding solid angle of the x-ray beams are chosen based on the tradeoff between x-ray flux (larger solid angles are more flux-efficient) versus scatter and cost (smaller solid angles result in better SPR and lower detector cost). The absence of antiscatter grid may also result in better geometric detection efficiency, especially when considering direct conversion detector technology as well as detector cost reduction. Finally, since the detector is small, it can affordably be made more specialized and one can envision using an ultra-high-resolution detector, a photon-counting detector, etc. It is worth noting that photon-counting and multisource technologies go hand-in-hand since both favor short view times and high frame rates, both strive to extract the most information from a limited number of x-rays, and the virtual bowtie may help limit the dynamic range of detected signals, relaxing the count-rate requirements.

To estimate the SPR of the IGCT scanner, we performed simulations and measurements on a benchtop setup to find the relationship between beam collimation and SPR and then extrapolated this to the actual IGCT scanner. For the benchmark experiments, we used a 32 cm water phantom, 140 kVp tube voltage, a detector without antiscatter grid, and a 12.3 cm^2 beam cross section at isocenter. This setup is very similar to the IGCT system, but has even tighter collimation. Simulations and measurements both give a maximum SPR of 0.2 ± 0.02, or an SPR per unit cross section of $0.0155/\text{cm}^2$. Since the IGCT scanner has a beam cross section of 40 cm^2, we estimate the SPR for 140 kVp and 32 cm water to be 62%. This SPR is higher than desirable. The phantoms and animals scanned in later experiments are much smaller and will have much better SPR. For comparison, commercial third-generation CT scanners with 40 mm z-coverage and an 1D antiscatter grid have an SPR on the order of 20% for a 32 cm water phantom.

3.B. X-ray flux analysis

Perhaps the most critical challenge with inverse-geometry CT is its flux capability. First, the choice of cathode technology in the x-ray tube can limit available tube current for generating x-rays. While field emitters (such as carbon nanotubes) have several potential advantages, their proven electron current density in x-ray systems is relatively low.[41] Our IGCT system uses dispenser cathodes, which are capable of delivering significantly higher current density and a total electron beam current of more than 1000 mA. Since the anode is stationary relative to the cathodes in the multisource (as opposed to the rotating anode used in traditional x-ray tubes), the x-ray flux is primarily limited by the target thermal limits, which in turn depend on the focal spot size, the dwell time, and the focal spot location repeat time. We expect the eventual thermal limit to be on the order of 500 mA at 120 kVp for a 1×1 mm optical focal spot size (at a dwell time of approximately 10 μs with 1 ms repeat time), approximately a factor of two lower than a rotating anode x-ray tube.

Since all x-ray focal spots are activated sequentially, any given object voxel is only irradiated for a fraction of the scan time. We define the duty cycle as the fraction of the scan time that any part of the volume is actually scanned or irradiated by x-rays. This duty cycle can be computed in two different ways. One way is to compute the ratio between the imaged volume and the instantaneous x-ray beam coverage. For example, if the imaged volume has a 50 cm field-of-view diameter and 16 cm coverage, and the x-ray beams cover a radial range of 20 cm and a longitudinal range of 8 cm, then the duty cycle is $(20\times8\ \text{cm})/(50\times16\ \text{cm}) = 20\%$, or voxels are on average irradiated for only 20% of the scan time. Alternatively we can compute the duty cycle as the reciprocal of the number of focal spots, compensated for the degree of overlap between neighboring x-ray beams. For example, for a system with 20 focal spots and a fourfold degree of overlap between the neighboring x-ray beams, the duty cycle is $1/(20/4) = 20\%$. The x-ray flux losses due to this duty cycle effect can be partially compensated by activating some focal spots more often or longer than others (electronic bowtie principle). The stationary anode and the duty cycle effect are the two key reasons why an IGCT scanner has limited flux capability. The stationary anode results in a low maximum x-ray source power. The duty cycle factors in to evaluate the effective x-ray source power, as seen by a given voxel.

In summary, by combining all the above effects, we expect that an optimized inverse-geometry system still has a significantly lower total flux capability than state-of-the-art third-generation scanners. Techniques such as model-based iterative reconstruction and photon-counting detectors can help to make images acceptable at this lower flux regime when slower scan times are not an option.

Despite its limited flux capability, IGCT offers a unique dose advantage, thanks to the virtual bowtie, described in Sec. 2.C. This mode of operation may still make IGCT a preferred choice for certain clinical applications, where maximum power is not an issue (such as for large patients) but dose-efficiency is most critical (such as for pediatric patients).

3.C. Experimental results

Experiments were performed in two modes: a first series of experiments were performed using a single source module

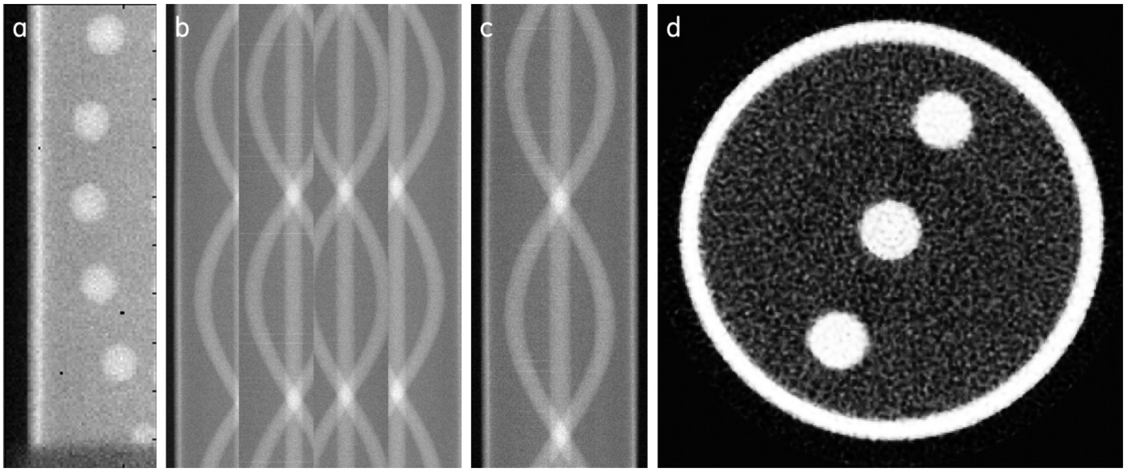

FIG. 4. Experimental results for the acrylic cylinder phantom with low-density foam and embedded acrylic spheres: (a) projection image corresponding to a single source, (b) sinograms for four different sources, (c) a merged sinogram, and (d) a reconstructed image (window = 1100 HU, level = 550 HU) (Reprinted with permission from De Man *et al.*, "Multi-source inverse-geometry CT: From system concept to research prototype," in IEEE Nuclear Science Symposium and Medical Imaging Conference, Orlando, Florida, 2009. Copyright 2009 IEEE).

(i.e., 2×4 focal spots) with careful mechanical balancing and 1 s gantry rotation. A second series of experiments were performed with four source modules (32 focal spots) with stationary gantry and 8 s phantom rotation. In all cases, below images were reconstructed using rebinning, FDK reconstruction, and image-domain weighted averaging.

A 70 mm diameter phantom was designed consisting of an acrylic mantel, which is filled with low-density foam and three embedded acrylic spheres. Figure 4 shows (a) a projection image corresponding to a single source, (b) sinograms for four different sources, (c) a merged sinogram, and (d) a reconstructed image, respectively. The reconstructed images do not show any significant image artifacts.

To measure the in-plane modulation transfer function (MTF), a 200 μm diameter tungsten wire (aligned parallel and positioned closely to the axis of rotation) was scanned. A volume of $3.75 \times 3.75 \times 3.5$ cm^3, centered at isocenter, was reconstructed with a voxel size of $0.15 \times 0.15 \times 0.14$ mm^3; in the reconstruction process, we used a Hanning window kernel filter with a cutoff of 34 lp/cm. To minimize the estimation error caused by image noise, a Gaussian function was fitted to the point spread function (PSF) in the central axial slice of the reconstructed volume.[42] To confirm that this level of spatial resolution is expected based on the nominal geometry of the IGCT system, we also "simulated" the in-plane MTF. Projection data were calculated using a numerical reprojector for a 200 μm diameter wire, using 17 by 17 subsamples to model the finite focal spot size and the finite detector cell size, and not including any physics effects (beam hardening, scatter, etc.).

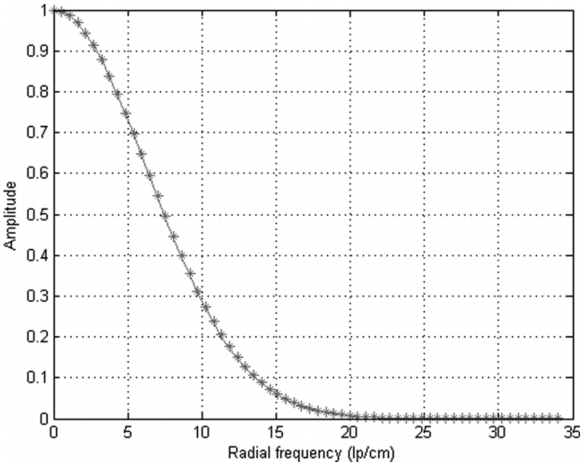

FIG. 5. MTF measurement for a 200 μm wire positioned near the rotation center. There is a close correspondence between measured (solid line) and simulated MTFs (* symbols) [Reproduced with permission from Baek *et al.*, "A multi-source inverse-geometry CT system: Initial results with an 8 spot x-ray source array," Phys. Med. Biol. **59**(5), 1189–1202 (2014). Copyright 2014 IOP Publishing].

The measured and simulated in-plane MTF values were compared, showing very good agreement (Fig. 5). The 10% MTF cutoff frequency was estimated to be 13 lp/cm. While spatial resolution is not a major advantage of IGCT, the smaller focal spot size in our experimental IGCT scanner results in a measured spatial resolution that is better than today's clinical scanners, which have a standard kernel spatial resolution on the order of 8–10 lp/cm. A minor benefit of an IGCT system is the fact that the apparent focal spot size is more consistent throughout the imaging volume. In third-generation CT scanners, the apparent focal spot width increases toward the edges of the fan-beam. In IGCT, since each focal spot is associated with a very small fan-beam, this resolution degrading effect is essentially absent.

To demonstrate the system performance for more complex, anatomical objects, a postmortem rat was scanned. The source voltage was 80 kVp, the source current was 125 mA, the exposure time per source per view was 5.4 μs, and the number of views per source was 125 over a 360°/1 s gantry rotation, so taking into account the 3-fold redundancy between the x-ray beams of adjacent sources, the effective mAs was $125\ \text{mA} \times 5.4\ \mu\text{s} \times 125 \times 3 = 0.25$ mAs (see Sec. 3.B for a full explanation on how we calculate the redundancy factor).

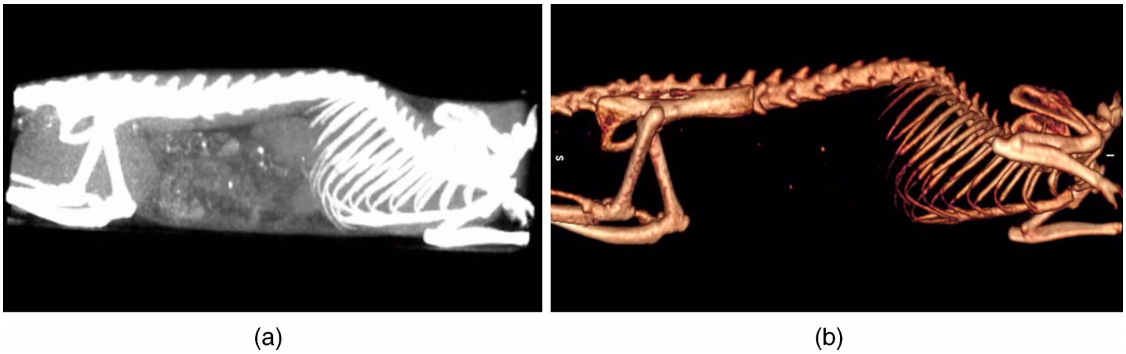

Fig. 6. Volume-rendered IGCT scan of a postmortem rat: (a) soft tissue window and (b) bone window.

Figures 6(a) and 6(b) show volume-rendered images of the rat using a soft tissue and bone window, respectively. These first preclinical images have visually acceptable image quality. These initial results, using a single source module (a 2×4 array of x-ray sources), demonstrate the feasibility of IGCT imaging, yielding large volumetric coverage with good image quality.

Subsequent experiments were performed using the final system configuration with 32 x-ray sources, using a rotating phantom stage, keeping the gantry stationary. First images were obtained from various simple and anatomical phantoms. We also scanned a rabbit, in a water-filled PMMA cylinder, subsequently frozen to keep the rabbit stationary relative to the rotating PMMA cylinder. The source voltage was 80 kVp, the source current was 80 mA, the exposure time per source per view was 100 μs, and the number of views per source was 300 over a 360°/8 s phantom rotation, so taking into account the 3-fold redundancy between the x-ray beams of adjacent sources, the effective mAs was approximately 7 mAs. Figure 7 shows a series of cross-sectional images of the rabbit in the ice-filled PMMA cylinder. This experiment demonstrates the 22 cm FOV of the 32-source system. The image quality is still suboptimal because of the low current used and the limited calibration efforts performed to date for the 32-spot source. Improved image quality could be achieved by pushing the source to its full beam current entitlement, refining the calibrations, applying advanced iterative reconstruction methods, and investigating more complex virtual bowtie modulation schemes.

We did not observe any significant cone-beam artifacts in any of the phantom scans, thanks to the multiaxial acquisition. At the same time, we did not perform an extensive cone-beam artifact study based on the IGCT scanner. The benefit of multiple offset x-ray sources for reduction of cone-beam artifacts was presented in detail in Refs. 7, 8, 12, and 13.

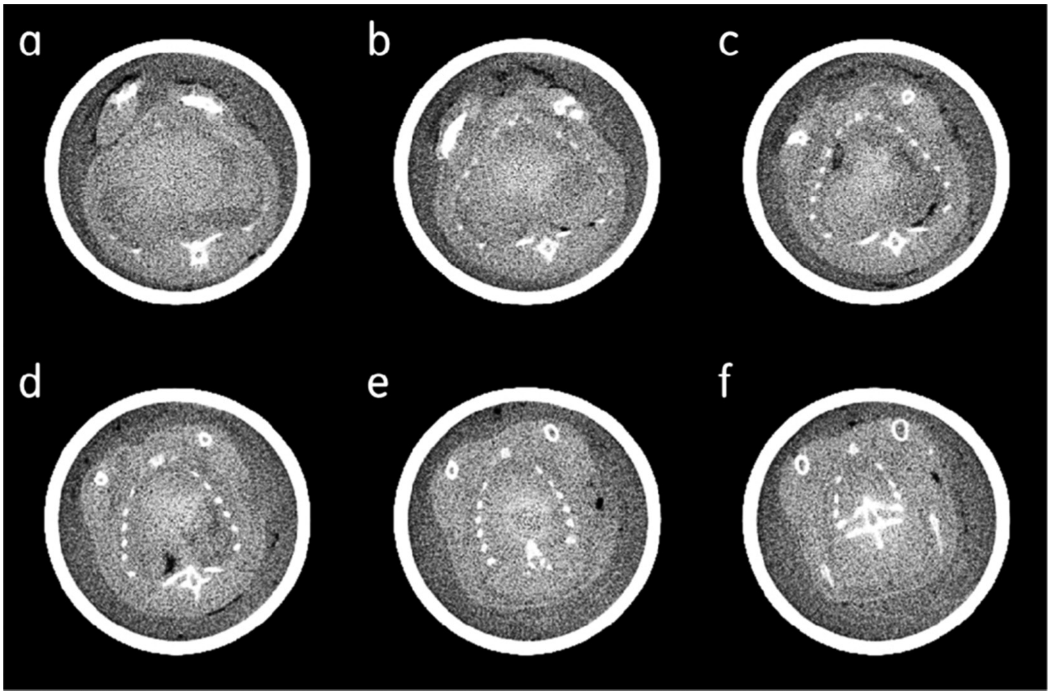

Fig. 7. Six *trans*axial slices of an IGCT scan of a rabbit, embedded in an ice-filled PMMA cylinder. In this case, the extended 32-spot source was used, corresponding to a 22 cm FOV (window = 500 HU, level = 900 HU).

4. CONCLUSIONS

We reported on the concept of multisource inverse-geometry CT and provided a summary of the design and development of an experimental gantry-based IGCT prototype. This development required significant innovation and collaborative effort from several disciplines: CT system design, mechanical design, component manufacturing, assembly and balancing, high-voltage controls design and system integration, logic controls design and system integration, distributed x-ray source development, detector design, assembly and integration, calibration development, reconstruction development, experimental data acquisition, calibration, reconstruction, and evaluation.

The development of a gantry-based IGCT scanner brought to light a variety of challenges, which in turn gave rise to numerous algorithmic and hardware solutions. The experimental results illustrate the general feasibility of multisource IGCT and at the same time highlight some of its current shortcomings. A major potential benefit of the IGCT geometry is its dose-efficiency, primarily because of the virtual bowtie concept, but also because of the potentially improved detector efficiency (with the elimination of the antiscatter grid). Together, these two improvements may reduce the dose by 0%–80%, depending on the patient anatomy, which is important for reducing risk of adverse patient impact due to x-ray radiation. A second benefit is the large axial coverage with reduced impact of cone-beam, heel effect, and other artifacts, which could make it easier to scan an entire heart or brain in a single rotation, without image quality compromises. The potential for cost reduction (due to reduced detector size and absence of antiscatter grid) is probably not realistic due to the additional cost of the distributed source. The biggest challenge for IGCT is delivering sufficient x-ray flux to achieve the required imaging image quality, given the thermal limits of a stationary target, the narrow beam collimation, and the limited number of focal spots. Only a large number of focal spots (to better distribute the thermal load) and a very high frame rate (to reduce the dwell time) may bring us into the flux regimes (and image quality) of today's commercial CT scanners. However, this need for higher flux capability will be somewhat reduced by current trends in CT imaging to reduce x-ray radiation dose by leveraging iterative statistical reconstruction techniques. A second challenge is the increased amount of scatter due to the absence of an antiscatter grid. The recent surge in compressed sensing research may give the IGCT architecture a unique advantage in terms of their ability to generate more random sampling patterns. However, we have not yet studied this combination and it is not clear whether compressed sensing techniques will also further relax the x-ray flux requirements.

Hence, future research may focus on the combination of IGCT and photon-counting detectors (further improving dose efficiency) and an increased number of focal spots. A more balanced IGCT design with a smaller distributed source and a larger detector (e.g., both on the order of 25 cm in-plane) deserves more investigation: it may offer optimized reconstruction strategies and allow firing of multiple sources simultaneously. Similarly, IGCT variations with multiple beam-lines would offer an advantage in either temporal resolution or improved flux, but at the expense of increased system complexity. Finally, inverse geometry CT system concepts with a stationary source and a rotating detector are being investigated as an alternative to this IGCT architecture.[43]

ACKNOWLEDGMENTS

This work was supported in part by NIH NIBIB Grant Nos. R01 EB006837 and R01 EB006837S (supplement), as well as by GE Healthcare and GE Global Research. The authors would like to especially acknowledge the scientists that contributed to the development of the IGCT system that are not listed as coauthors of this paper, including, with Stanford University: Samuel Mazin, Tally Schmidt, and Arunduti Ganguly; with GE Global Research: Maria Iatrou, Colin Wilson, Kedar Khare, Peter Sanza, Bernard Claus, Thomas Benson, Xiaodong Tao, Eric Tkaczyk, Paul FitzGerald, Brendon Tower, Jim LeBlanc, William Ross, Samit Basu, and Cameron Ritchie; with GE Healthcare: Julie Schwab, Bob Reneau, Chad Smith, Ray Shawn, Steve Wolocheck, and Jim Dodge; and with Triple Ring: Ed Solomon.

CONFLICT OF INTEREST DISCLOSURE

The authors have no COI to report.

---

[a] Author to whom correspondence should be addressed. Electronic mail: deman@ge.com

[1] W. Wagner, "Device for measuring local radiation absorption in a body," U.S. patent 4,057,725 (November 8, 1977).
[2] W. Berninger and R. Redington, "Multiple purpose high speed tomographic x-ray scanner," U.S. patent 4,196,352 (April 1, 1980).
[3] J. Hsieh, "Dual cardiac CT scanner," U.S. patent 6,421,412 (July 16, 2002).
[4] T. Flohr *et al.*, "First performance evaluation of a dual-source CT (DSCT) system," Eur. Radiol. **16**, 256–268 (2006).
[5] H. Xu, "Study of single-rotation direct volume imaging with trough-like x-ray source," Ph.D. dissertation, Shanghai Jiao Tong University, 2002.
[6] T. G. Schmidt, R. Fahrig, E. G. Solomon, and N. J. Pelc, "An inverse-geometry volumetric CT system with a large area scanned source: A feasibility study," Med. Phys. **31**(9), 2623–2627 (2004).
[7] T. G. Schmidt, R. Fahrig, and N. J. Pelc, "A three-dimensional reconstruction algorithm for an inverse geometry volumetric CT system," Med. Phys. **32**(11), 3234–3245 (2005).
[8] T. G. Schmidt, J. Star-Lack, N. R. Bennett, S. R. Mazin, E. G. Solomon, R. Fahrig, and N. J. Pelc, "A prototype table-top inverse-geometry volumetric CT system," Med. Phys. **33**, 1867–1878 (2006).
[9] T. Albert, "Large-area scanning x-ray source to maximize contrast sensitivity by minimizing scatter detection," Proc. SPIE **2009**, 164743 (1993).
[10] E. Solomon *et al.*, "Scanning-beam digital x-ray (SBDX) system for cardiac angiography," Proc. SPIE **3659**, 349499 (1999).
[11] B. De Man *et al.*, "Method and system for imaging using multiple offset x-ray emission points," U.S. Patent 7,639,775 (December 29, 2009).
[12] Z. Yin and B. De Man, "Cone beam artifact reduction using multiple axial acquisitions," *World Congress of Medical Physics*, *Seoul*, *2006*.
[13] Z. Yin, B. De Man, and J. Pack, "Analytical cone-beam reconstruction using a multi-source inverse geometry CT system," Proc. SPIE **6510**, 651021 (2007).
[14] D. Bequé, B. De Man, and M. Iatrou, "Iterative reconstruction for multi-source inverse geometry CT: A feasibility study," Proc. SPIE **6510**, 65105Y (2007).

[15] Z. Yin and B. De Man, "3D analytic cone-beam reconstruction for less than a full scan using a multi-source CT system," *IEEE Nuclear Science Symposium and Medical Imaging Conference*, *Honolulu*, *2007*.

[16] M. Iatrou, B. De Man, D. Beque, Z. Yin, T. Benson, and K. Khare, "3D iterative full scan and half scan reconstruction in CT architectures with distributed sources," Proc. SPIE **6913**, 691322 (2008).

[17] J. Baek and N. J. Pelc, "A new reconstruction method to improve SNR for an inverse geometry CT system," Proc. SPIE **6913**, 69132Z (2008).

[18] Z. Yin, B. De Man, J. Pack, and K. Khare, "3D analytic cone-beam reconstruction for multi-axial CT acquisitions," Int. J. Biomed. Imaging **2009**, 1–11.

[19] J. Baek and N. J. Pelc, "Direct two-dimensional reconstruction algorithm for an inverse-geometry CT system," Med. Phys. **36**(2), 394–401 (2009).

[20] J. Baek and N. J. Pelc, "A new method to combine 3D reconstruction volumes for multiple parallel circular cone beam orbits," Med. Phys. **37**, 5351–5360 (2010).

[21] D. Beque, B. De Man, J. Uribe, and W. Waters, "Geometrical calibration of multi-source inverse geometry CT systems using a wire phantom," *IEEE Nuclear Science Symposium and Medical Imaging Conference*, *Dresden, Germany*, *2008*.

[22] J. Baek, N. Pelc, B. De Man, J. Uribe, D. Harrison, J. Reynolds, B. Neculaes, L. Inzinna, and A. Caiafa, "Initial results with a multi-source inverse-geometry CT system," Proc. SPIE **8313**, 83131A (2012).

[23] J. Baek *et al.*, "A multi-source inverse-geometry CT system: Initial results with an 8 spot x-ray source array," Phys. Med. Biol. **59**(5), 1189–1202 (2014).

[24] J. Baek, B. De Man, D. Harrison, and N. Pelc, "Raw data normalization for a multi source inverse geometry CT system," Opt. Express **23**(6), 7514–7526 (2015).

[25] B. De Man, S. Basu, D. Bequé, B. Claus, P. Edic, M. Iatrou, J. LeBlanc, B. Senzig, R. Thompson, M. Vermilyea, C. Wilson, Z. Yin, and N. Pelc, "Multi-source inverse geometry CT: A new system concept for x-ray computed tomography," Proc. SPIE **6510**, 65100H (2007).

[26] B. De Man, S. Basu, P. Fitzgerald, D. Harrison, M. Iatrou, K. Khare, J. LeBlanc, B. Senzig, C. Wilson, Z. Yin, and N. Pelc, "Inverse geometry CT: The next generation CT architecture?," *IEEE Nuclear Science Symposium and Medical Imaging Conference*, *Honolulu*, *2007*.

[27] B. De Man, N. Pelc, C. Dumoulin, and T. Bernstein, "Propagation of quantum noise in multiplexed x-ray imaging," Proc. SPIE **6913**, 69131U (2008).

[28] Z. Yin and B. De Man, "An experimental study of multi-source inverse geometry CT," *IEEE Nuclear Science Symposium and Medical Imaging Conference*, *Dresden, Germany*, *2008*.

[29] B. De Man, A. Caiafa, Y. Cao, K. Frutschy, D. Harrison, L. Inzinna, R. Longtin, B. Neculaes, J. Reynolds, J. Roy, J. Short, J. Uribe, W. Waters, Z. Yin, X. Zhang, Y. Zou, B. Senzig, J. Baek, and N. Pelc, "Multi-source inverse-geometry CT: From system concept to research prototype," *IEEE Nuclear Science Symposium and Medical Imaging Conference*, *Orlando, Florida*, *2009*.

[30] B. De Man, J. Uribe, R. Longtin, D. Harrison, J. Reynolds, B. Neculaes, K. Frutschy, L. Inzinna, A. Caiafa, R. Senzig, J. Baek, and N. Pelc, "Multisource inverse-geometry CT: Progress update and image noise analysis," *CT Meeting*, *Salt Lake City, UT*, *2010*.

[31] J. Uribe, J. Reynolds, L. Inzinna, R. Longtin, D. Harrison, B. De Man, B. Neculaes, A. Caiafa, W. Waters, K. Frutschy, R. Senzig, J. Baek, and N. Pelc, "Multi-source inverse-geometry CT: Prototype system integration," *IEEE Nuclear Science Symposium and Medical Imaging Conference*, *Knoxville, TN*, *2010*.

[32] J. Uribe, J. Reynolds, R. Longtin, D. Harrison, W. Waters, B. De Man, B. Neculaes, K. Frutschy, L. Inzinna, A. Caiafa, J. Baek, and N. Pelc, "First imaging with gantry-based multisource inverse geometry CT scanner," *RSNA*, *Chicago*, *2010*.

[33] B. De Man, B. Senzig, B. Claus, D. Beque, J. Miller, X. Tao, and P. Mendonca, "Computer assisted scan protocol and reconstruction (CASPAR)," *RSNA*, *Chicago*, *2007*.

[34] J. Sperl, D. Bequé, B. Claus, B. De Man, B. Senzig, and M. Brokate, "Computer assisted scan protocol and reconstruction (CASPAR)—Reduction of image noise and patient dose," IEEE Trans. Med. Imaging **29**(3), 724–732 (2010).

[35] S. Bartolac, S. Graham, J. Siewerdsen, and D. Jaffray, "Fluence field optimization for noise and dose objectives in CT," Med. Phys. **38**(7), S2–S17 (2011).

[36] T. P. Szczykutowicz and C. A. Mistretta, "Experimental realization of fluence field modulated CT using digital beam attenuation," Phys. Med. Biol. **59**, 1305–1326 (2014).

[37] V. Robinson, W. Smith, X. Rui, Z. Yin, M. Wu, P. Fitzgerald, and B. De Man, "Experimental demonstration of a dynamic bowtie for region-based CT fluence optimization," Proc. SPIE **9783**, 97833G (2016).

[38] J. Hsieh, *Computed Tomography Principles, Design, Artifacts, and Recent Advances*, 2nd ed. (Wiley, 2009).

[39] L. A. Feldkamp *et al.*, "Practical cone-beam algorithm," J. Opt. Soc. Am. A **1**(6), 612–619 (1984).

[40] X. Tang, J. Hsieh, A. Hagiwara, R. A. Nilsen, J.-B. Thibault, and E. Drapkin, "A three-dimensional weighted cone beam filtered backprojection (CB-FBP) algorithm for image reconstruction in volumetric CT under a circular source trajectory," Phys. Med. Biol. **50**, 3889–3905 (2005).

[41] X. Qian *et al.*, "Design and characterization of a spatially distributed multibeam field emission x-ray source for stationary digital breast tomosynthesis," Med. Phys. **36**(10), 4389–4399 (2009).

[42] E. L. Nickoloff and R. Riley, "A simplified approach for modulation transfer function determinations in computed tomography," Med. Phys. **12**(4), 437–442 (1985).

[43] S. S. Hsieh, J. A. Heanue, T. Funk, W. S. Hinshaw, B. P. Wilfley, E. G. Solomon, and N. J. Pelc, "The feasibility of an inverse geometry CT system with stationary source arrays," Med. Phys. **40**(3), 031904 (2013).

[44] V. B. Neculaes *et al.*, "Multisource inverse-geometry CT. Part II. X-ray source design and prototype," Med. Phys. **43**, 4617–4627 (2016).